EFFICIENT METHODS TO SIMULATE PLANAR FREE SURFACE IN THE 3D 4TH-ORDER STAGGERED-GRID FINITE-DIFFERENCE SCHEMES

JOZEF KRISTEK[1], PETER MOCZO[1,2] AND RALPH. J. ARCHULETA[3]

ABSTRACT

We numerically tested accuracy of two formulations of Levander's (1988) stress-imaging technique for simulating a planar free surface in the 4th-order staggered-grid finite-difference schemes. We have found that both formulations (one with normal stress-tensor components at the surface, the other with shear stress-tensor components at the surface) require at least 10 grid spacings per minimum wavelength ($\lambda_{min}/h = 10$) if Rayleigh waves are to be propagated without significant grid dispersion in the range of epicentral distances up to 15 λ^S_{dom}.

Because interior 4th-order staggered-grid schemes usually do not require more than 6 grid spacings per minimum wavelength, in the considered range of epicentral distances, it was desirable to find alternative techniques to simulate a planar free surface, which would not require denser spatial sampling than $\lambda_{min}/h = 6$. Therefore, we have developed and tested new techniques: 1. Combination of the stress imaging (with the shear stress-tensor components at the surface) with Rodrigues' (1993) vertically refined grid near the free surface. 2. Application of the adjusted finite-difference approximations to the z-derivatives at the grid points at and below the surface that uses no virtual values above the surface and no stress imaging. The normal stress-tensor components are at the surface in one formulation, while the shear stress-tensor components are at the surface in the other formulation.

The three developed formulations give for the spatial sampling $\lambda_{min}/h = 6$ results very close to those obtained by the discrete-wavenumber method. Because, however, the technique with the vertically refined grid near the free surface requires 3 times smaller time step (due to the refined grid), the technique with adjusted finite-difference approximations is the most accurate and efficient technique from the examined formulations in the homogeneous halfspace.

1 Geophysical Institute, Slovak Academy of Sciences, Dúbravská cesta 9, 842 28 Bratislava, Slovak Republic

2 Department of Geophysics, Faculty of Mathematics, Physics and Informatics, Comenius University, Mlynská dolina F1, 842 48 Bratislava, Slovak Republic

3 Institute for Crustal Studies, University of California at Santa Barbara, Santa Barbara, CA 93106, USA

1. INTRODUCTION

The finite-difference (FD) method is a key numerical tool in the recent numerical modeling of earthquake ground motion. Accuracy of the finite-difference modeling strongly depends on the implementation of the free-surface (i.e., traction-free) condition.

Obviously, a free-surface topography (nonplanar free surface) is more difficult to simulate than a planar free surface, however, even the planar free surface is not easy to simulate sufficiently accurately. In this paper we consider only numerical simulation of the planar horizontal free surface. A concise review of the modeling of the free-surface topography until 1996 can be found, e.g., in the paper by *Moczo et al. (1997)*. Later development is reflected in, e.g., *Hestholm (1999)*, *Hestholm et al. (1999)* and *Ruud and Hestholm (2001)*.

Here, we consider only staggered-grid FD schemes which became the most popular FD schemes soon after *Virieux (1984, 1986)* applied *Madariaga's (1976)* method to the wave propagation problem.

In the staggered-grid FD schemes, the horizontal free surface can be placed either at the horizontal grid plane with grid positions of the normal stress-tensor components or plane with grid positions of the shear stress-tensor components.

Levander (1988) suggested using virtual values of the stress-tensor components above the free surface and apply the antisymmetry condition for the stress-tensor components about the free surface. He applied this technique to his 2D P-SV 4^{th}-order staggered-grid velocity-stress FD scheme. We call Levander's technique the stress-imaging technique throughout this study. It is not clear from Levander's paper which stress-tensor components are placed at the free surface and how virtual particle velocities above the free surface are treated.

Rodrigues (1993) developed a 3D 8^{th}-order staggered-grid displacement-stress scheme and used the stress-imaging technique with the normal stress-tensor components at the free surface. He found that it is necessary to take 10 to 15 grid points per shortest wavelength to avoid a significant numerical dispersion. Therefore, he combined the stress-imaging technique with a vertically refined grid near the free surface and achieved good accuracy.

Graves (1996) applied the stress-imaging technique with the normal stress-tensor components at the free surface in his 3D 4^{th}-order staggered-grid velocity-stress modeling. Graves gave a clear explanation of treatment of the stress-tensor and particle-velocity components at and above the free surface. He found this technique better than the alternative vacuum formulation approach which applies the interior FD scheme also to the free-surface grid points and assumes zero density and elastic moduli above the free surface.

Ohminato and Chouet (1997) focused in their paper on a free-surface topography, however, their technique is relevant also to the planar free-surface modeling because they preferred to locate the shear stress-tensor components at the free surface in their 3D 2^{nd}-order staggered-grid displacement-stress modeling.

Graves (unpublished data) tested the accuracy of the two formulations in his 3D 4^{th}-order staggered-grid velocity-stress scheme in a homogeneous halfspace against the frequency wavenumber integration method. Graves used minimum sampling of 5 grid points per shear wavelength. He also compared grid phase and group velocities as

functions of grid points per shear wavelength with the theoretical curves. Based on the numerical tests he found the formulation with the normal stress-tensor components at the free surface better than the other formulation.

Gottschämmer and Olsen (2001) tested accuracy of the two formulations in the 3D 4^{th}-order staggered-grid velocity-stress scheme in a homogeneous halfspace against the discrete-wavenumber method of *Bouchon (1981)*. They used 'a Gaussian-shaped function corresponding to approximately 6 points per shear wavelength'. Gottschämmer and Olsen showed cases when one formulation is better than the other and vice-versa. They concluded with the recommendation to use the formulation with the shear stress-tensor components at the free surface and to apply averaging across the free surface in order to obtain values of the horizontal components of the particle velocity at the free surface.

In this paper we first numerically test accuracy of the two formulations by comparing them with the discrete-wavenumber method. Based on the tests we present two alternative techniques to simulate a planar free surface in the staggered-grid FD schemes.

2. PROBLEM FORMULATION

Consider a 3D Cartesian coordinate system (x, y, z) with the x-axis horizontal and positive to the right and the z-axis positive downward. Also consider a perfectly elastic isotropic halfspace for $z \geq 0$ with a planar free surface at $z = 0$. Let density ρ, shear modulus μ and bulk modulus κ be functions of x, y, z. Let displacement vector $\vec{u}(u, v, w)$, stress tensor $\tau_{\varepsilon\gamma}$; $\varepsilon, \gamma \in \{x, y, z\}$, and body force per unit volume $\vec{f}(f_x, f_y, f_z)$ be functions of x, y, z and time t. The equations of motion are

$$\rho\ddot{u} = \tau_{xx,x} + \tau_{yx,y} + \tau_{zx,z} + f_x$$

$$\rho\ddot{v} = \tau_{xy,x} + \tau_{yy,y} + \tau_{zy,z} + f_y$$

$$\rho\ddot{w} = \tau_{xz,x} + \tau_{yz,y} + \tau_{zz,z} + f_z \qquad (1)$$

and Hooke's law is

$$\tau_{xx} = \kappa\theta + \frac{2}{3}\mu\left(2u_{,x} - v_{,y} - w_{,z}\right)$$

$$\tau_{yy} = \kappa\theta + \frac{2}{3}\mu\left(-u_{,x} + 2v_{,y} - w_{,z}\right)$$

$$\tau_{zz} = \kappa\theta + \frac{2}{3}\mu\left(-u_{,x} - v_{,y} + 2w_{,z}\right)$$

$$\tau_{xy} = \tau_{yx} = \mu\left(u_{,y} + v_{,x}\right)$$

$$\tau_{yz} = \tau_{zy} = \mu\left(v_{,z} + w_{,y}\right)$$

$$\tau_{zx} = \tau_{xz} = \mu\left(w_{,x} + u_{,z}\right) \tag{2}$$

where θ is volume dilatation

$$\theta = u_{,x} + v_{,y} + w_{,z} \tag{3}$$

and $\ddot{u} = \partial^2 u / \partial t^2$, $\tau_{xx,x} = \partial \tau_{xx} / \partial x$, $u_{,x} = \partial u / \partial x$, etc.

The traction vector $\vec{T}\left(\vec{u},\vec{n}\right)$,

$$\left[T_x, T_y, T_z\right] = \left[n_x, n_y, n_z\right] \begin{bmatrix} \tau_{xx} & \tau_{xy} & \tau_{xz} \\ \tau_{yx} & \tau_{yy} & \tau_{yz} \\ \tau_{zx} & \tau_{zy} & \tau_{zz} \end{bmatrix} \tag{4}$$

is equal to zero at the free surface at $z = 0$ with a unit normal vector $\vec{n}(0,0,-1)$. Therefore,

$$\tau_{zx} = \tau_{zy} = \tau_{zz} = 0 \tag{5}$$

is the boundary condition at the free surface.

Equations (1) and (2) can be solved by a FD method. Fig. 1 shows a FD grid cell of the staggered-grid scheme. U and T_{xy} represent FD approximations to u (or, possibly, $\partial u / \partial t$) and τ_{xy}, etc. Quantities $\rho_U, ..., \mu_{xy}, ...,$ and κ represent grid material parameters.

In the 4th-order staggered-grid FD schemes, the first spatial derivative of some function $\varphi(\xi)$ at $\xi = \xi_0$ is approximated by

$$\varphi_{,\xi}(\xi_0) = \frac{1}{h}\left\{a\left[\varphi\left(\xi_0 + \frac{3}{2}h\right) - \varphi\left(\xi_0 - \frac{3}{2}h\right)\right] + b\left[\varphi\left(\xi_0 + \frac{1}{2}h\right) - \varphi\left(\xi_0 - \frac{1}{2}h\right)\right]\right\} \tag{6}$$

with $a = -1/24$, $b = 9/8$ and h being a grid spacing. Formula (6) would give a 2nd-order approximation formula if $a = 0$ and $b = 1$.

It is obvious that there are at least two options for localizing the free surface with respect to the staggered spatial grid. In the first approach we place the free surface at the horizontal grid plane going through the positions of the horizontal displacement components U, V, and stress-tensor components T_{xx}, T_{yy}, T_{zz} and T_{xy}. In the second one, the free surface coincides with the horizontal grid plane going through the positions of W, T_{zx} and T_{zy}. For brevity, we will use mnemonic denotation – the H formulation (with the horizontal displacement/particle velocity components at the free surface) for the first and

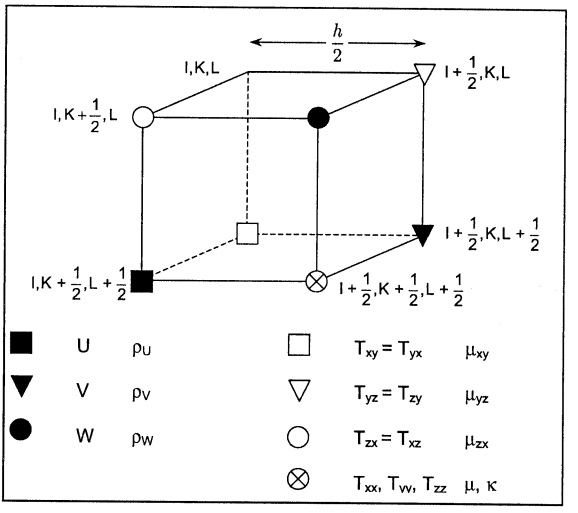

Fig. 1. A finite-difference (FD) grid cell with positions of the wavefield variables and effective material parameters.

W formulation (with vertical displacement/particle velocity components at the free surface) for the second option.

3. THE STRESS-IMAGING TECHNIQUE

As the equation (1) and (2), and the FD approximation formula (6) indicate, the update of the displacement and stress-tensor components at the free surface and grid planes at $z = h/2$ and $z = h$ according to the FD scheme for interior grid points requires values of the displacement and stress-tensor components at grid planes $z = -h/2$, $z = -h$ and $z = -3h/2$, i.e., above the free surface. The technique suggested originally by *Levander (1988)* for the 2D P-SV 4th-order velocity-stress FD scheme and well described for the 3D case by *Graves (1996)* can be called the stress-imaging technique. In principle, the technique applies explicit boundary conditions to the stress-tensor components located at the free surface and uses imaged values for the stress-tensor components above the free surface assuming their antisymmetry about the free surface. The antisymmetry,

$$\tau_{zx}(-z) = -\tau_{zx}(z)$$

$$\tau_{zy}(-z) = -\tau_{zy}(z)$$

$$\tau_{zz}(-z) = -\tau_{zz}(z) \qquad (7)$$

assures that

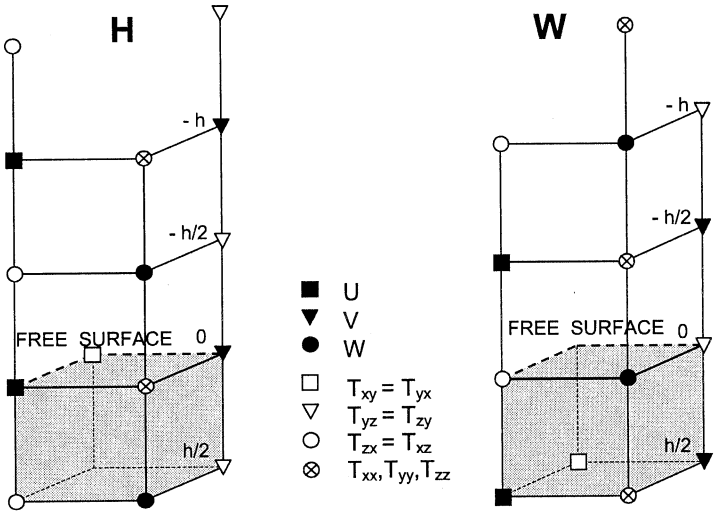

Fig. 2. Left: A surface FD grid cell, position of the free surface, and virtual field quantities required above the free surface in the H formulation of the standard stress-imaging technique. Right: The same for the W formulation.

$$\tau_{zx}(0) = \tau_{zy}(0) = \tau_{zz}(0) = 0$$

as required by the boundary condition (5).

3.1. The H formulation

The positions of the free surface and quantities required above the free surface are shown in Fig. 2 (left). The explicit application of the boundary conditions, imaged values of the stress-tensor components, and computed values of the displacement components above the free surface are summarized in Table 1. Treatment of the quantities not listed in Table 1 is the same as in the case of interior grid points.

3.2. The W formulation

The positions of the free surface and quantities required above the free surface are shown in Fig. 2 (right). Analogously to the case of the H formulation, the W formulation is summarized in Table 2.

3.3. Theoretical comparison of the H and W formulations

Although the principle is the same for the both formulation, looking at Table 1 and 2 we see clear differences from which one could intuitively guess that the two formulations might yield different results. The differences are summarized in Table 3.

Obviously, a rigorous theoretical analysis of stability and grid dispersion of the two formulations at least in a homogenous halfspace would be desirable. Such analysis is not trivial. Therefore, we performed extensive numerical simulations and comparisons of the two formulations.

3.4. Numerical comparison of the H and W formulations

We tested accuracy of the both formulations against the discrete-wavenumber (DWN) method (*Bouchon, 1981*; computer code *Axitra by Coutant, 1989*) which is very accurate and often used as the reference solution. The FD computations were performed using the 3D 4th-order staggered-grid displacement-stress FD scheme (*Moczo et al., 2000, 2001*). Note that in the case of the homogeneous halfspace there is no difference between the used and any other 3D 4th-order staggered-grid FD scheme in a material parameterization. We also checked our calculations against the velocity-stress FD scheme and found no difference.

Model. A perfectly elastic isotropic homogenous halfspace with the S-wave velocity $b = 3000$ m/s, density $r = 1500$ kg/m^3 and the P-wave velocity either $a = 5200$ m/s or $a = 9950$ m/s. The lower and higher P-wave velocities correspond to two values of Poisson's ratio – $s = 0.25$ and $s = 0.45$, respectively.

Table 1. Summary of the H formulation

$T_{zz}(0) = 0$	
$T_{xx}(0)$	is obtained from the 4th-order FD approximation to Hooke's law for τ_{xx} in which derivative $w_{,z}$ is replaced by derivatives $u_{,x}$ and $v_{,y}$ according to condition $\tau_{zz}(0) = 0$ and Hooke's law for τ_{zz}.
$T_{yy}(0)$	the same as above but for τ_{yy}.
$T_{zx}(-h/2) = -T_{zx}(h/2)$,	$T_{zy}(-h/2) = -T_{zy}(h/2)$
$T_{zz}(-h) = -T_{zz}(h)$	
$T_{zx}(-3h/2) = -T_{zx}(3h/2)$,	$T_{zy}(-3h/2) = -T_{zy}(3h/2)$
$U(0)$	is obtained from the 4th-order FD approximation to the equation of motion in which $\tau_{zx,z}$ is obtained also using imaged τ_{zx} values.
$V(0)$	the same as above but with $\tau_{zy,z}$ and τ_{zy}.
$W(-h/2)$	is obtained from the 2nd-order FD approximation to the condition $\tau_{zz}(0) = 0$ and Hooke's law for τ_{zz}.
$U(-h)$	is obtained from the 2nd-order FD approximation to the antisymmetry condition $\tau_{zx}(-h/2) = -\tau_{zx}(h/2)$ and Hooke's law for τ_{zx}.
$V(-h)$	the same as above but with τ_{zy}.

Table 2. Summary of the W formulation

$T_{zx}(0) = 0,$ $\quad T_{zy}(0) = 0$

$T_{zz}(-h/2) = -T_{zz}(h/2)$

$T_{zx}(-h) = -T_{zx}(h),$ $\quad T_{zy}(-h) = -T_{zy}(h)$

$T_{zz}(-3h/2) = -T_{zz}(3h/2)$

$W(0)$	is obtained from the 4th-order FD approximation to the equation of motion in which $\tau_{zz,z}$ is obtained also using imaged τ_{zz} values.
$U(-h/2)$	is obtained from the 2nd-order FD approximation to the condition $\tau_{zx}(0) = 0$ and Hooke's law for τ_{zx}.
$V(-h/2)$	is obtained from the 2nd-order FD approximation to the condition $\tau_{zy}(0) = 0$ and Hooke's law for τ_{zy}.
$W(-h)$	is obtained from the 2nd-order FD approximation to the condition of the antisymmetry $\tau_{zz}(-h/2) = -\tau_{zz}(h/2)$ and Hooke's law for τ_{zz}.

Table 3. Comparison of the H and W formulations

H formulation	W formulation
At the free surface	
1 directly prescribed stress-tensor component	2 directly prescribed stress-tensor components
2 displacement components calculated using 4 imaged stress-tensor components	1 displacement component calculated using 2 imaged stress-tensor components
Needed above the free surface	
5 imaged stress-tensor components 3 displacement components calculated using the 2nd-order scheme	4 imaged stress-tensor components 3 displacement components calculated using the 2nd-order scheme

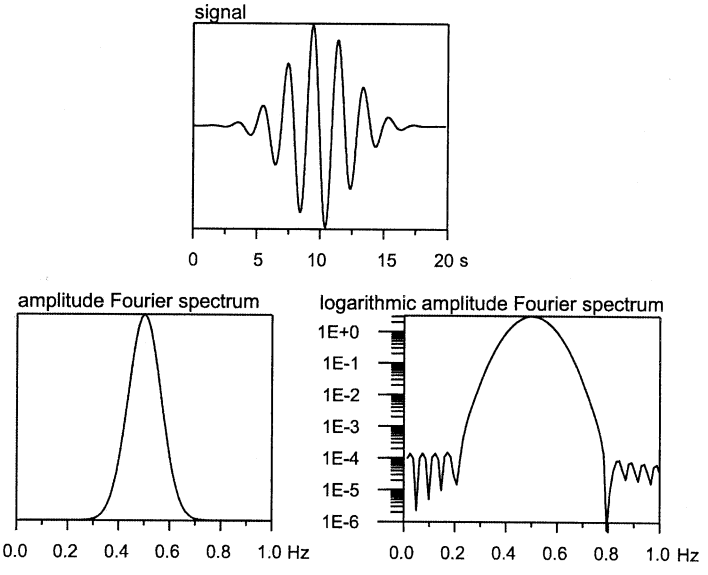

Fig. 3. Gabor signal used in the numerical simulations and its amplitude Fourier spectrum.

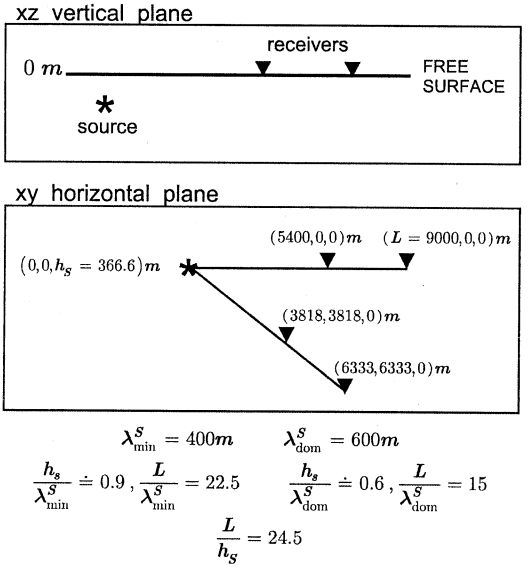

Fig. 4. The source-receiver configuration shown schematically in the *xz* vertical and *xy* horizontal planes. Star denotes a point double-couple source, triangle denotes a receiver. Only two receivers are depicted here for which synthetic velocity seismograms are shown in the next figures. The dominant and minimum S-wave wavelengths as well as their ratios to the maximum epicentral distance and source depth are also shown.

Source. A point double-couple source with dip $\delta = 90°$, rake $\lambda = 0°$ and strike either $\phi_S = 45°$ or $\phi_S = 0°$. A source time function corresponds to slip velocity and is given by Gabor wavelet

$$s(t) = \exp\left\{-[\omega(t - t_S)/\gamma]^2\right\} \cos[\omega(t - t_S) + \psi]$$

with $\omega = 2\pi f_P$ and $t_S = 0.45\gamma/f_P$. Because in the standard theoretical analysis stability and grid dispersion are analyzed for a harmonic signal we chose $f_P = 0.5$ Hz, $\gamma = 11$ and $\psi = \pi/2$ which give a relatively narrow-spectrum signal (shown in Fig. 3). Thus, in the chosen model of the medium, the dominant and minimum wavelengths of the S wave are $\lambda^S_{dom} = 600$ m and $\lambda^S_{\min} = 400$ m, respectively. The depth of the source, $h_S = 366.6$ m, was chosen relatively small, $h_S / \lambda^S_{\min} \doteq 0.9$, in order to allow for efficient generation of Rayleigh waves.

Source-receiver configuration. Receiver positions were chosen so that comparison of the wave propagation in the direction of a coordinate axis coinciding with a grid line and that in the direction of the horizontal plane diagonal be possible. Epicentral distances in both directions range from $3\,\lambda^S_{dom}$ to $15\,\lambda^S_{dom}$. The source-receiver configuration is schematically shown in Fig. 4. Given this configuration, the source with strike $\phi_S = 45°$ generates efficient Rayleigh wave propagation in the direction of the x-axis and SH wave propagation in the direction of the diagonal. The source with strike $\phi_S = 0°$ interchanges directions of propagation of the two types of waves.

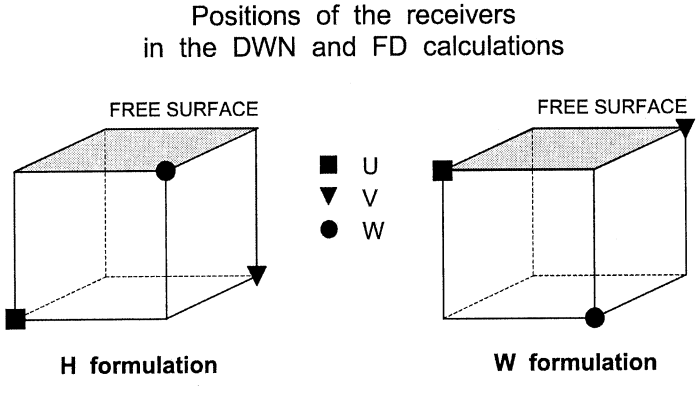

Fig. 5. Positions of receivers for the U, V and W components of displacement/particle velocity used in both the DWN (discrete-wavenumber) and FD calculations. In other words, the DWN and FD solutions refer to exactly the same spatial positions.

Let us emphasize that in each DWN calculation we considered 3 receivers in order to exactly fit the positions of the u, v and w components of the displacement/particle velocity in the staggered grid in the FD calculations. In other words, there is no averaging between different receiver positions or inaccuracy due to half-grid spacing shift in receiver positions (see Fig. 5).

Results. Part of the numerical calculations performed for all combinations of the above mentioned parameters is illustrated in Figs. 6, 7 and 8. Figure 6 shows synthetic velocity seismograms computed by the FD method with the H formulation and those computed by the DWN method. Seismograms are shown for the source with $\phi_S = 45°$, $\delta = 90°$ and $\lambda = 0°$ which generates efficient Rayleigh wave propagation in the direction of the x-axis and SH wave propagation in the direction of the horizontal diagonal. (The case of $\phi_S = 0°$, $\delta = 90°$ and $\lambda = 0°$ was also investigated but is not shown in the paper.) The top and bottom parts of the figure show seismograms for Poisson's ratios $\sigma = 0.25$ and $\sigma = 0.45$, respectively, both for the sampling ratio $\lambda_{\min}/h = 6$. Figure 7 shows the same for the W formulation. Figure 8 compares the H and W formulations with the DWN solutions for the case with $\sigma = 0.25$ and $\lambda_{\min}/h = 10$.

The analysis of all numerical calculations leads to the following conclusions for the sampling ratio $\lambda_{\min}/h = 6$:

1. The P and SH-wave propagation is modeled sufficiently accurately by both the W and H formulations. (Obviously, sufficient accuracy is a relative, problem-dependent concept. The observed level of agreement between the DWN and FD solutions might be interpreted as sufficient accuracy of the FD solution in the earthquake ground motion modeling.)
2. While the W formulation causes a delay of Rayleigh waves, the H formulation causes an earlier arrival of Rayleigh waves.
3. The W formulation gives better amplitudes of Rayleigh waves.
4. There is no significant anisotropy in the grid – propagation in the direction of the grid line and diagonal are close.
5. There is no significant dependence of accuracy of both formulations on Poisson's ratio.

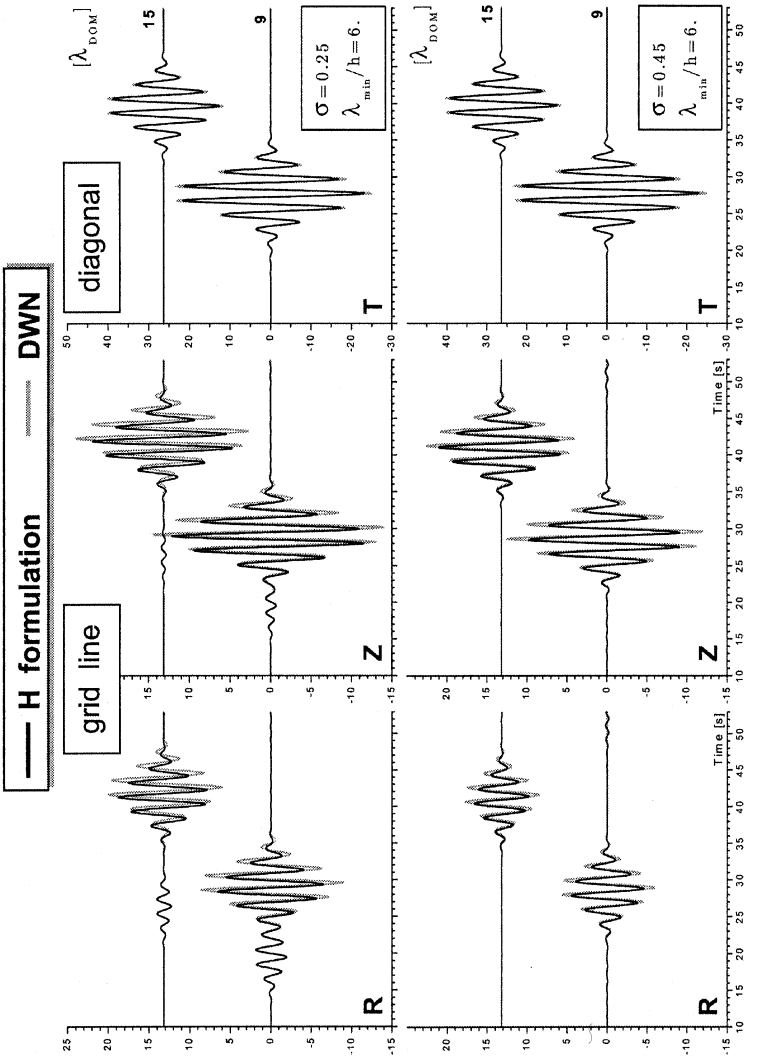

Fig. 6. Synthetic velocity seismograms calculated by the H formulation and DWN method for two values of Poisson's ratio (0.25 and 0.45). Sampling ratio 6 grid spacings per minimum wavelength was is used in the FD calculation. The double couple source generates Rayleigh wave propagation in the direction of the grid line and SH propagation along the horizontal diagonal. R, Z and T denote radial (U), vertical (-W) and transverse ([V–U] /√2) components.

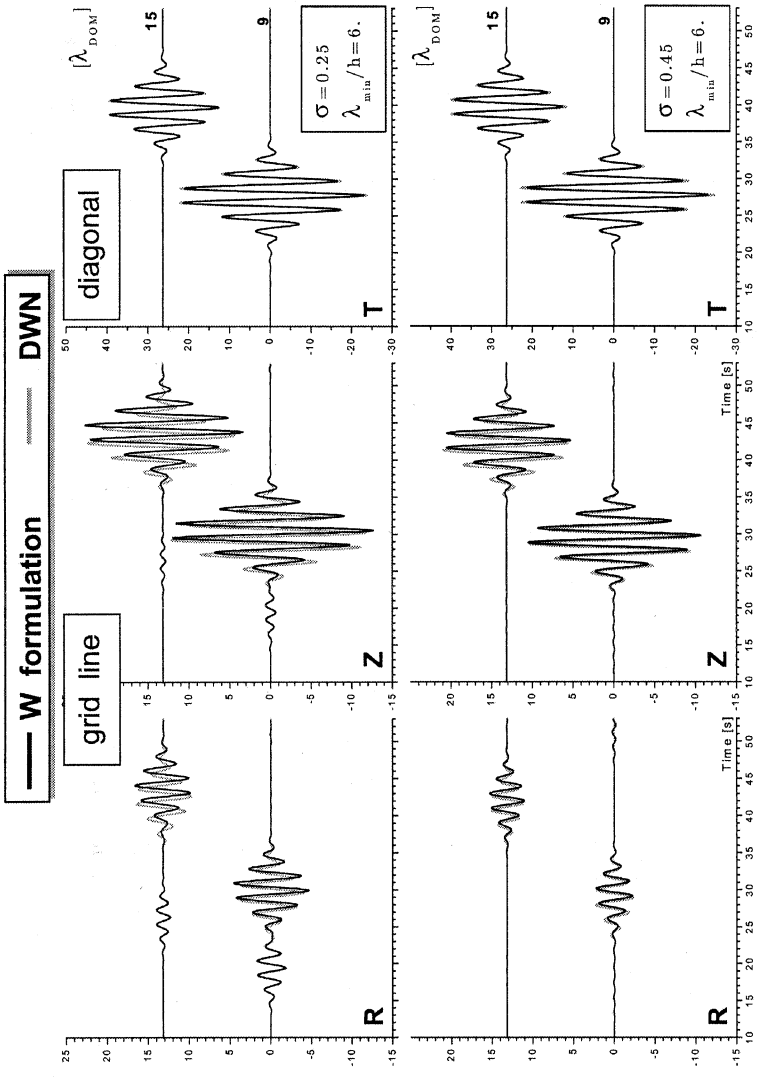

Fig. 7. The same as in Fig. 6 but for the W formulation.

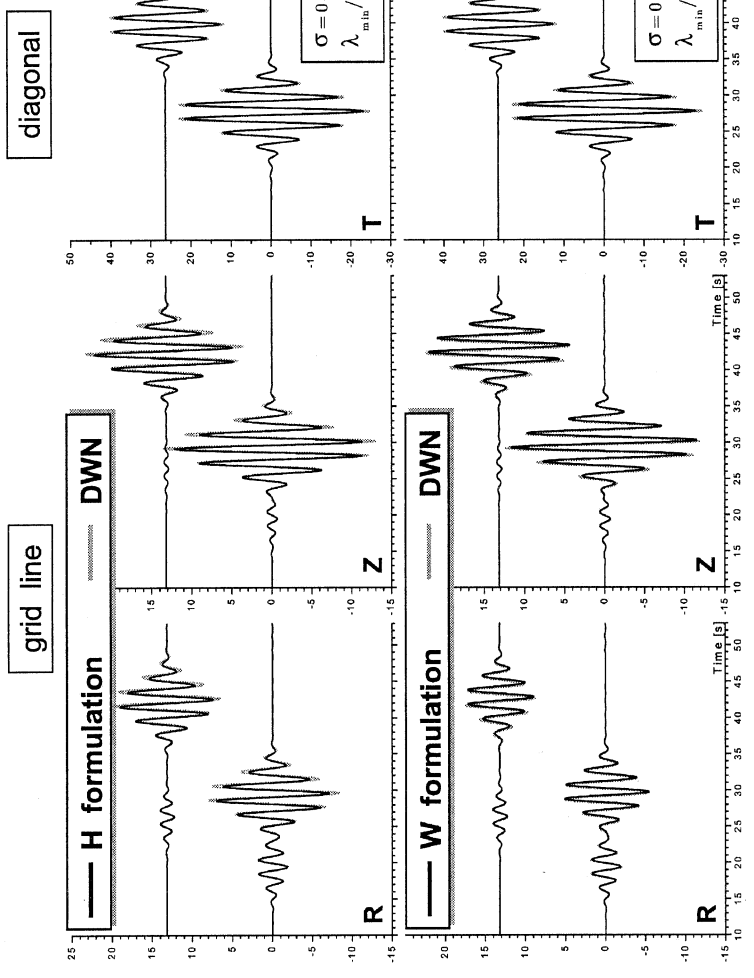

Fig. 8. Synthetic velocity seismograms calculated by the H (top panel) and W (bottom panel) formulation compared with those calculated by the DWN method. Poisson's ratio is 0.25. Sampling ratio 10 grid spacings per minimum wavelength is used in both the FD calculations.

The main conclusions from all calculations for the sampling ratios $\lambda_{\min}/h = 6$ and $\lambda_{\min}/h = 10$ are:

a. At least 10 grid spacings per wavelength (i.e., $\lambda_{\min}/h = 10$) are necessary in order to achieve sufficient accuracy in modeling Rayleigh wave propagation by the both formulations.
b. If $\lambda_{\min}/h = 10$, the W formulation gives better amplitudes while the H formulation gives better phases.

The consequence of the two above conclusions is obvious: Application of either of the two formulations requires sampling ratio at least 10 grid spacings per minimum wavelength which is much more than that (6 grid spacing per minimum wavelength; see *Moczo et al., 2000*) required by the 4th-order FD schemes in an unbounded medium. This would, however, significantly reduce the efficiency of the 4th-order FD modeling. Therefore, some other technique is desirable that would be sufficiently accurate at sampling ratio $\lambda_{\min}/h = 6$.

Let us stress that considering a particular value of the spatial sampling ratio $\lambda_{\min}/h$ is reasonable only for a given epicentral distance or range of the epicentral distances. Considering $\lambda_{\min}/h = 6$ or 10 in this study relates to the range of the epicentral distances up to $15\lambda^S_{dom}$. This range is well representative in the earthquake ground motion modeling in sedimentary valleys and basins.

4. THE W FORMULATION WITH A VERTICALLY REFINED GRID (W-VRG)

Rodrigues (1993) used a grid that was refined only in the vertical direction and only down to a necessary depth in his 8th-order velocity-stress FD modeling. In his modeling the normal stress-tensor components are located at the free surface which corresponds to what we call in this paper the H formulation. Because we think the W formulation is better than the H formulation, we combine Rodrigues' idea with the W formulation.

The principle of this technique, which we call W-VRG is:

- stress-imaging technique in the W formulation,
- vertically refined grid near the free surface,
- adjusted FD approximations to the z-derivatives at the grid points near the bottom of the refined grid.

The W-VRG technique is illustrated in Fig. 9. In addition to the horizontal grid planes at depths $h/2$, h and $3h/2$ (of the regular grid), there are 6 horizontal grid planes at depths $h/6$, $h/3$, $2h/3$, $5h/6$, $7h/6$ and $4h/3$. As a part of the refined grid, virtual horizontal grid planes above the free surface are also spaced with half grid spacing $h/3$. The z-derivatives are approximated by formula (6) at depths $3h/2$, $2h$, etc. The z-derivatives at depths $z_0 = 0, h/6, h/3, h/2, 2h/3, 5h/6$ and h are approximated by the 4th-order formula

$$\varphi_{,z}(z_0)=\frac{1}{h}\left\{a_1\left[\varphi\left(z_0+\frac{1}{2}h\right)-\varphi\left(z_0-\frac{1}{2}h\right)\right]+b_1\left[\varphi\left(z_0+\frac{1}{6}h\right)-\varphi\left(z_0-\frac{1}{6}h\right)\right]\right\} \quad (8)$$

with $a_1=-1/8$ and $b_1=27/8$, which is obtained from (6) after substitution of $h/3$ for h. The z-derivatives at depth $z_0=7h/6$ are approximated by the 4th-order formula

$$\varphi_{,z}(z_0)=\frac{1}{h}\left\{a_2\left[\varphi\left(z_0+\frac{5}{6}h\right)-\varphi\left(z_0-\frac{5}{6}h\right)\right]+b_2\left[\varphi\left(z_0+\frac{1}{3}h\right)-\varphi\left(z_0-\frac{1}{3}h\right)\right]\right\} \quad (9)$$

with $a_2=-1/120$ and $b_2=25/24$. The z-derivatives at depth $z_0=4h/3$ are approximated by the 4th-order formula

$$\varphi_{,z}(z_0)=\frac{1}{h}\left\{a_3\left[\varphi\left(z_0+\frac{2}{3}h\right)-\varphi\left(z_0-\frac{2}{3}h\right)\right]+b_3\left[\varphi\left(z_0+\frac{1}{6}h\right)-\varphi\left(z_0-\frac{1}{6}h\right)\right]\right\} \quad (10)$$

with $a_3=-1/336$ and $b_3=49/48$.

Figure 10 shows synthetic velocity seismograms calculated by the W-VRG technique and those calculated by the DWN method (compare with the top panels of Figs. 6 and 7). It is clear from this and other calculations (not shown here) that the W-VRG technique with only 6 grid spacings per minimum wavelength gives results close to those obtained by the DWN method.

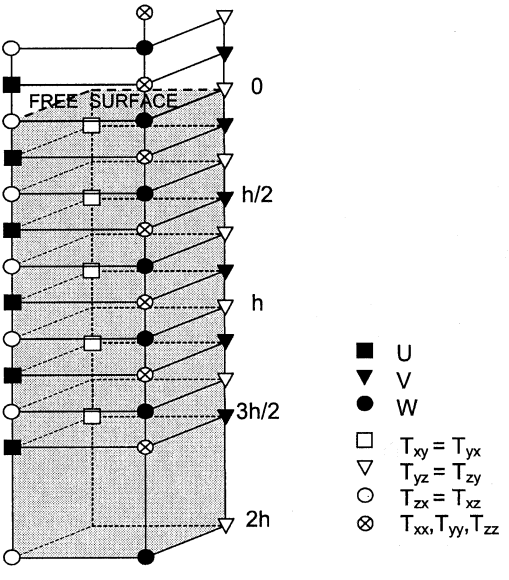

Fig. 9. A part of the FD grid, position of the free surface, and virtual field quantities required above the free surface in the W-VRG technique which combines the W formulation of the standard stress-imaging technique with a vertically refined grid.

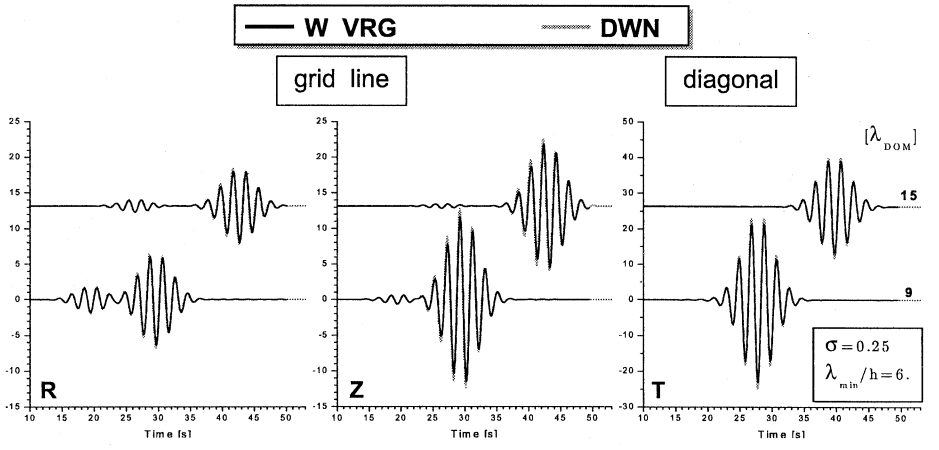

Fig. 10. Synthetic velocity seismograms calculated by the W-VRG technique and DWN method for Poisson's ratio 0.25. Sampling ratio 6 grid spacings per minimum wavelength was is used in the FD calculation. The double couple source generates Rayleigh wave propagation in the direction of the grid line and SH propagation along the horizontal diagonal. R, Z and T denote radial (U), vertical (-W) and transverse ([V–U] /√2) components.

5. THE H AND W FORMULATIONS WITH THE ADJUSTED FD APPROXIMATIONS (H-AFDA AND W-AFDA)

The traction-free surface can be simulated in the staggered-grid FD scheme alternatively – without the stress imaging. As in the case of the standard stress imaging and stress imaging combined with the vertically refined grid, there are two possible formulations. In one formulation, the normal stress-tensor components, τ_{xy} and the u and v components of the displacement are located at the free surface. In the other formulation, the shear stress-tensor components τ_{zx} and τ_{zy}, and the w component of the displacement are located at the free surface. The principle of our approach is:

- directly prescribed zero values of τ_{zz} at the free surface in the first formulation or τ_{zx} and τ_{zy} in the second formulation,
- no stress imaging: i.e., no virtual stress-tensor and displacement components above the free surface,
- adjusted FD approximations to the z-derivatives at the grid points at and below the free surface.

We can call the two techniques based on the above principle as the H and W formulations with the adjusted FD approximations and use acronyms H-AFDA and W-AFDA. The techniques are illustrated in Fig. 11. The treatment of the stress-tensor and displacement components at the free surface and depths $h/2$ and h in the H-AFDA is summarized in

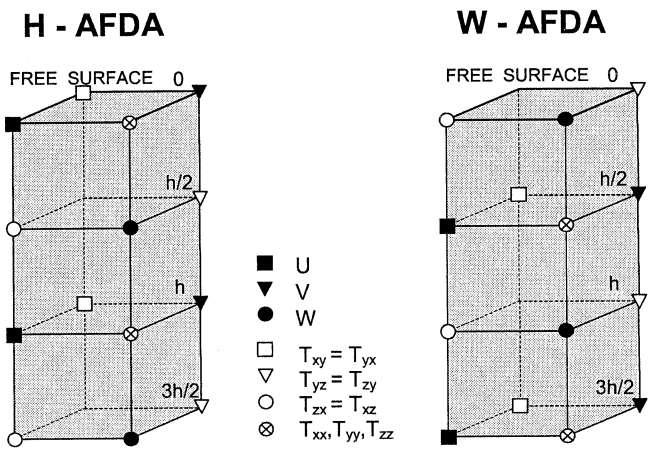

Fig. 11. Left: A part of the FD grid and position of the free surface in the H-AFDA technique. The z-derivatives at the free surface and depths of $h/2$, h and $3h/2$ are calculated using adjusted FD approximations given in Table 6. Right: The same for the W-AFDA technique.

Table 4. Similarly, the treatment of the stress-tensor and displacement components at the free surface and depths $h/2$ and h in the W-AFDA is summarized in Table 5. The FD approximation formulas (#1 – #4), used in the both formulations, are listed in Table 6.

Fig. 12 shows synthetic velocity seismograms calculated by the H-AFDA and W-AFDA techniques and those calculated by the DWN method (compare with the top panels of Figs. 6 and 7 and Fig. 10). The H-AFDA and W-AFDA seismograms were also calculated for other model configurations used for comparison of the W and H formulations of the standard stress imaging (not shown here). Both the H-AFDA and W-AFDA techniques with only 6 grid spacings per minimum wavelength give results close to those obtained by the DWN method. The W-AFDA gives better amplitudes while the H-AFDA gives better phases. This is similar comparison as that between the H and W formulations of the standard stress imaging in the case of 10 grid spacings per minimum wavelength.

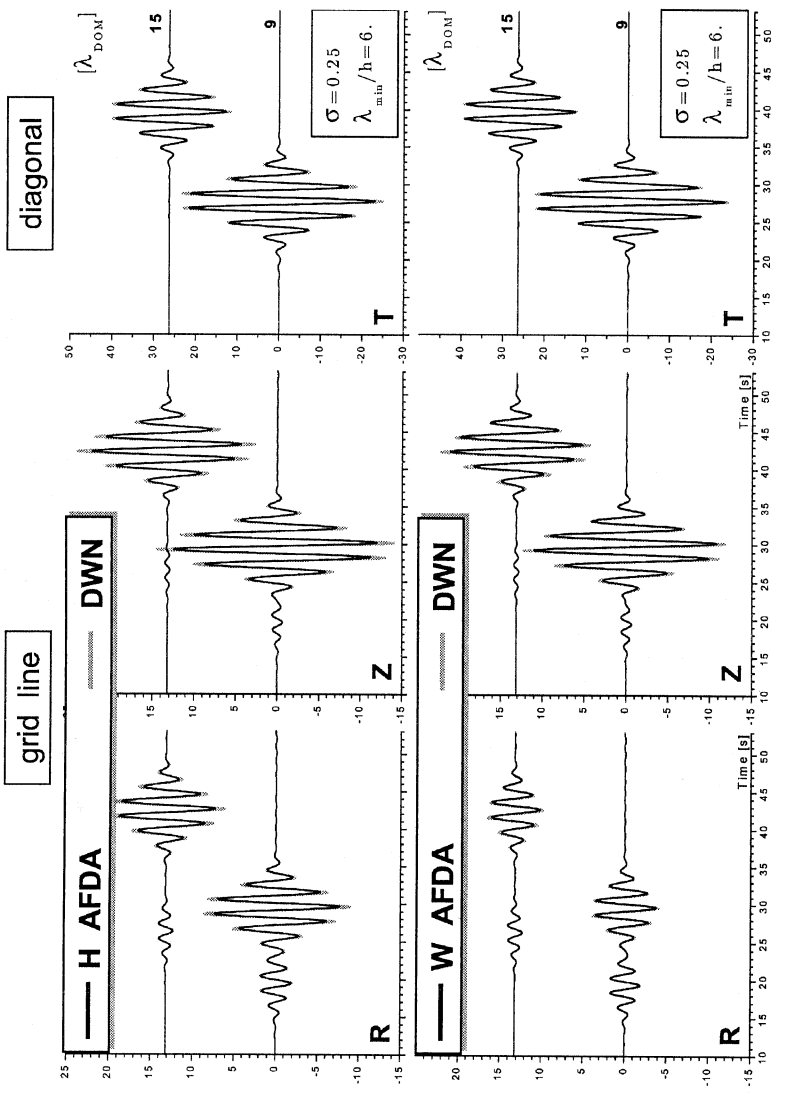

Fig. 12. Synthetic velocity seismograms calculated by the H-AFDA (top panel) and W-AFDA (bottom panel) techniques compared with those calculated by the DWN method. Poisson's ratio is 0.25. Sampling ratio 6 grid spacings per minimum wavelength is used in both the FD calculations.

Table 4. Summary of the H-AFDA technique

$T_{zz}(0)=0$	
$T_{xx}(0)$	is obtained from the 4th-order FD approximation to Hooke's law for τ_{xx}; derivative $w,_z$ is replaced by derivatives $u,_x$ and $v,_y$ due to condition $\tau_{zz}(0)=0$.
$T_{yy}(0)$	similar to $T_{xx}(0)$.
$T_{zx}(h/2)$	is obtained from the 4th-order FD approximation to Hooke's law for τ_{zx}; derivative $u,_z$ is approximated by formula #2.
$T_{zy}(h/2)$	is obtained from the 4th-order FD approximation to Hooke's law for τ_{zy}; derivative $v,_z$ is approximated by formula #2.
$T_{xx}(h)$	is obtained from the 4th-order FD approximation to Hooke's law for τ_{xx}; derivative $w,_z$ is approximated by formula #3 in which $w,_z(0)$ is replaced by derivatives $u,_x$ and $v,_y$ due to condition $\tau_{zz}(0)=0$.
$T_{yy}(h)$ and $T_{zz}(h)$	– similar to $T_{xx}(h)$.
$U(0)$	is obtained from the 4th-order FD approximation to the equation of motion for u; derivative $\tau_{zx},_z$ is approximated by formula #1 in which condition $\tau_{zx}(0)=0$ is used.
$V(0)$	is obtained from the 4th-order FD approximation to the equation of motion for v; derivative $\tau_{yz},_z$ is approximated by formula #1 in which condition $\tau_{yz}(0)=0$ is used.
$W(h/2)$	is obtained from the 4th-order FD approximation to the equation of motion for w; derivative $\tau_{zz},_z$ is approximated by formula #2.
$U(h)$	is obtained from the 4th-order FD approximation to the equation of motion for u; derivative $\tau_{zx},_z$ is approximated by formula #4 in which condition $\tau_{zx}(0)=0$ is used.
$V(h)$	is obtained from the 4th-order FD approximation to the equation of motion for v; derivative $\tau_{yz},_z$ is approximated by formula #4 in which condition $\tau_{yz}(0)=0$ is used.

Table 5. Summary of the W-AFDA technique

$T_{zx}(0)=0,$	$T_{zy}(0)=0$
$T_{xx}(h/2)$	is obtained from the 4th-order FD approximation to Hooke's law for τ_{xx}; derivative $w_{,z}$ is approximated by formula #2.
$T_{yy}(h/2)$ and $T_{zz}(h/2)$	– similar to $T_{xx}(h/2)$
$T_{zx}(h)$	is obtained from the 4th-order FD approximation to Hooke's law for τ_{zx}; derivative $u_{,z}$ is approximated by formula #3 in which $u_{,z}(0)$ is replaced by $w_{,x}$ due to condition $\tau_{zx}(0)=0$.
$T_{zy}(h)$	is obtained from the 4th-order FD approximation to Hooke's law for τ_{zy}; derivative $v_{,z}$ is approximated by formula #3 in which $v_{,z}(0)$ is replaced by $w_{,y}$ due to condition $\tau_{zy}(0)=0$.
$W(0)$	is obtained from the 4th-order FD approximation to the equation of motion for *w*; derivative $\tau_{zz,z}$ is approximated by formula #1 in which condition $\tau_{zz}(0)=0$ is used.
$U(h/2)$	is obtained from the 4th-order FD approximation to the equation of motion for *u*; derivative $\tau_{zx,z}$ is approximated by formula #2.
$V(h/2)$	is obtained from the 4th-order FD approximation to the equation of motion for *v*; derivative $\tau_{zy,z}$ is approximated by formula #2.
$W(h)$	is obtained from the 4th-order FD approximation to the equation of motion for *w*; derivative $\tau_{zz,z}$ is approximated by formula #4 in which condition $\tau_{zz}(0)=0$ is used.

Table 6. FD approximation formulas used in the H-AFDA and W-AFDA techniques

formula #1

$$f'(z_0)=\frac{1}{h}\left[-\frac{352}{105}f(z_0)+\frac{35}{8}f\left(z_0+\frac{h}{2}\right)-\frac{35}{24}f\left(z_0+\frac{3}{2}h\right)+\frac{21}{40}f\left(z_0+\frac{5}{2}h\right)-\frac{5}{56}f\left(z_0+\frac{7}{2}h\right)\right]+O\left(h^4\right)$$

formula #2

$$f'(z_0)=\frac{1}{h}\left[-\frac{11}{12}f\left(z_0-\frac{h}{2}\right)+\frac{17}{24}f\left(z_0+\frac{h}{2}\right)+\frac{3}{8}f\left(z_0+\frac{3}{2}h\right)-\frac{5}{24}f\left(z_0+\frac{5}{2}h\right)+\frac{1}{24}f\left(z_0+\frac{7}{2}h\right)\right]+O\left(h^4\right)$$

formula #3

$$f'(z_0)=\frac{1}{h}\left[-\frac{h}{22}f'(z_0-h)-\frac{577}{528}f\left(z_0-\frac{h}{2}\right)+\frac{201}{176}f\left(z_0+\frac{h}{2}\right)-\frac{9}{176}f\left(z_0+\frac{3}{2}h\right)+\frac{1}{528}f\left(z_0+\frac{5}{2}h\right)\right]+O\left(h^4\right)$$

formula #4

$$f'(z_0)=\frac{1}{h}\left[\frac{16}{105}f(z_0-h)-\frac{31}{24}f\left(z_0-\frac{h}{2}\right)+\frac{29}{24}f\left(z_0+\frac{h}{2}\right)-\frac{3}{40}f\left(z_0+\frac{3}{2}h\right)+\frac{1}{168}f\left(z_0+\frac{5}{2}h\right)\right]+O\left(h^4\right)$$

6. QUANTITATIVE EVALUATION OF ACCURACY

In general, it is better to evaluate accuracy of the numerical methods in a quantitative way using reasonably defined error criteria. Let $S(t)$ be the tested solution and $S_{REF}(t)$ the reference solution. Perhaps the simplest possible quantitative criterion is a difference D defined as

$$D(t) = S_{REF}(t) - S(t) \ .$$

An integral criterion, say, misfit M, can be defined as

$$M = \frac{\sqrt{\sum_m [S_{REF}(t_m) - S(t_m)]^2}}{\sqrt{\sum_m S_{REF}^2(t_m)}} .$$

Though both criteria are used in comparisons of two solutions, it is not difficult to check that they account more for a phase misfit than for an amplitude misfit. In order to evaluate both the accuracy in the amplitude and phase we define the envelope misfit EM as

$$EM = \frac{\sqrt{\sum_m \left[\left| \hat{S}_{REF}(t_m) \right| - \left| \hat{S}(t_m) \right| \right]^2}}{\sqrt{\sum_m \left| \hat{S}_{REF}(t_m) \right|^2}}$$

and the phase misfit PM as

$$PM = \frac{\sqrt{\sum_m \left[\left| \hat{S}_{REF}(t_m) \right| Arg\left(\hat{S}_{REF}(t_m) / \hat{S}(t_m) \right) \right]^2}}{\pi \cdot \sqrt{\sum_m \left| \hat{S}_{REF}(t_m) \right|^2}} ,$$

where $\hat{S}_{REF}(t)$ and $\hat{S}(t)$ are analytical signals of $S_{REF}(t)$ and $S(t)$, respectively, and $Arg(\varphi)$ is the principal value of the argument of a complex quantity φ.

Figure 13 shows the envelope and phase misfits for the solutions shown in the previous figures for all tested and developed methods. It is very clear from Fig. 13 that the envelope and phase misfits for the transverse component of motion in all techniques and formulations are relatively small and close to each other. This is in agreement with the conclusion based on simple visual comparisons of the seismograms. The transverse motion in the simulations is due to the body SH wave propagation. We can conclude that all techniques and formulations model the body SH wave propagation in a homogeneous halfspace in the studied range of the epicentral distances comparably and sufficiently accurately.

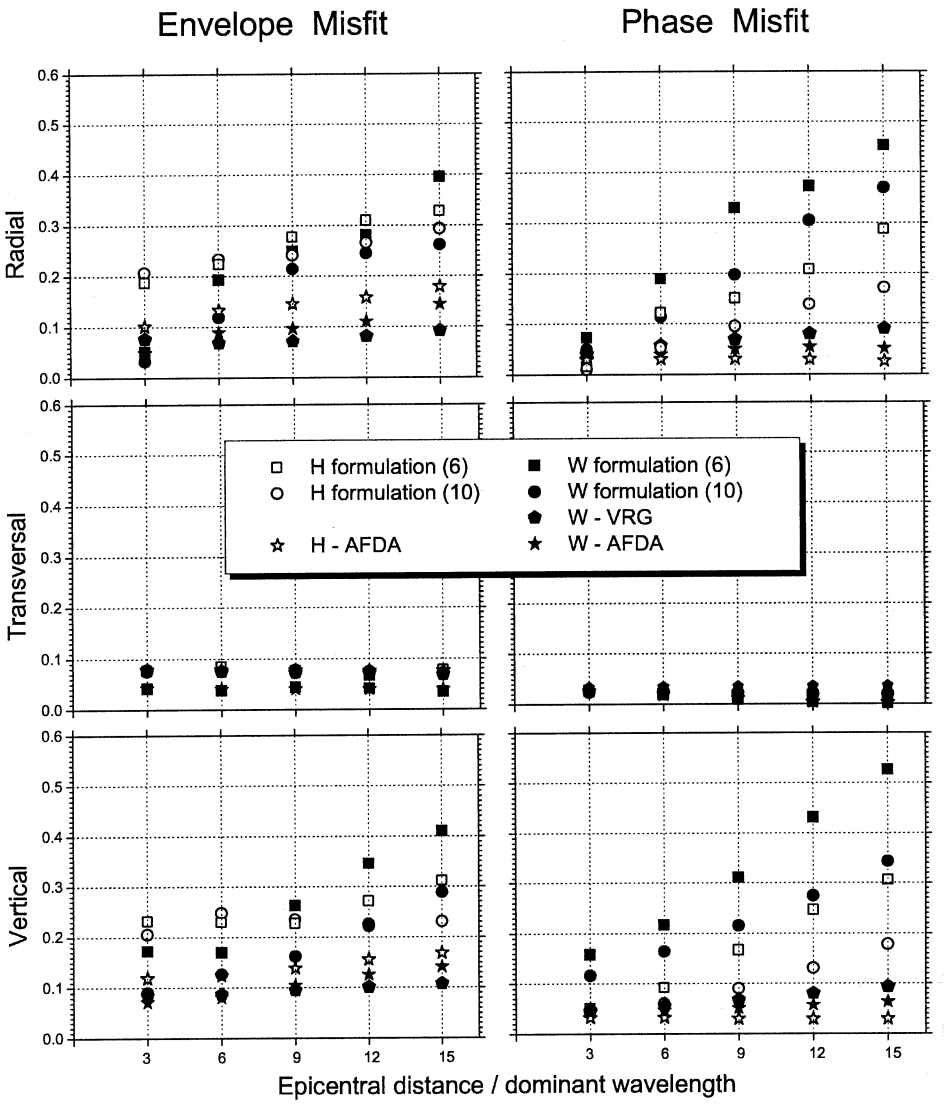

Fig. 13. Accuracy of the investigated and developed methods for simulation of the planar free surface. The envelope and phase misfits are evaluated against the normalized epicentral distance. The DWN solutions are used as the reference solutions. Numbers 6 and 10 mean the numbers of the grid spacings per minimum wavelength used in the H and W formulations of the standard stress-imaging technique. 6 grid spacing per minimum wavelength are used in the W-VRG, H-AFDA and W-AFDA solutions. Poisson's ratio is 0.25 in all cases.

The phase misfits of the radial and vertical components in the standard stress-imaging technique for a given epicentral distance, in the studied range of the epicentral distances, is smaller for $\lambda_{\min}/h=10$ than that for $\lambda_{\min}/h=6$. The phase misfit for a given epicentral distance and spatial sampling is smaller in the H formulation than that in the W formulation. This is in agreement with the conclusions based on simple visual comparisons of seismograms.

Analogous simple statements cannot be made for the envelope misfits in the standard stress-imaging technique. This is likely due to the fact that the envelope misfit also 'feels' the phase misfit.

Compare now the misfits of the three developed techniques – W-VRG, H-AFDA and W-AFDA. The phase misfit for a given epicentral distance is largest in the W-VRG and smallest in the H-AFDA solutions, though the values are relatively close to each other and all below 0.1 The envelope misfit for a given epicentral distance is largest in the H-AFDA and smallest in the W-VRG. For the studied epicentral distances the misfits are below 0.2.

Given the fact that the W-VRG technique requires a three times smaller time step we prefer the H-AFDA and W-AFDA techniques. Given smaller difference between phase misfits and larger difference between the envelope misfits of the two formulations in the radial component we conclude that the W-AFDA formulation as the slightly better of the two formulations.

7. CONCLUSIONS

We numerically tested two formulations of *Levander's (1988)* stress-imaging technique. In the H formulation the normal stress-tensor and horizontal displacement/particle velocity components are located at the free surface. In the W formulation the shear stress-tensor and vertical displacement/particle velocity components are located at the free surface. Comparison of the numerical results for a homogeneous halfspace with calculations by the discrete-wavenumber method show that both formulations require at least 10 grid spacings per minimum shear wavelength in order to achieve reasonable accuracy in modeling Rayleigh wave propagation in the range of the epicentral distances up to $15\,\lambda^{S}_{dom}$.

Because spatial sampling $\lambda_{\min}/h \geq 10$ obviously degrades efficiency of the 4th-order FD modeling to the 2nd-order level, we have developed two alternative techniques:

1. W-VRG: Combination of the W formulation of the stress imaging with Rodrigues' (1993) vertically refined grid near the free surface.
2. a) H-AFDA: H formulation (normal stress-tensor and horizontal displacement/ particle velocity components at the free surface) with adjusted FD approximations to the z-derivatives at the grid points at and below the free surface (the technique uses no virtual values above the free surface and no stress imaging).
   b) W-AFDA: W formulation (shear stress-tensor and vertical displacement/ particle velocity components at the free surface) with adjusted FD approximations to the z-derivatives at the grid points at and below the free surface (the technique uses no virtual values above the free surface and no stress imaging).

By numerically comparing the three developed formulations with the discrete-wavenumber method in the range of the epicentral distances up to 15 λ_{dom}^{S} we have found that for the spatial sampling $\lambda_{\min} / h = 6$ they give results very close to those obtained by the discrete-wavenumber method. However, because W-VRG requires 3 times smaller time step (due to the vertically refined grid near the free surface), we conclude that AFDA is the most accurate and efficient technique from the examined formulations in the homogeneous halfspace. While H-AFDA gives slightly better phases, W-AFDA gives better amplitudes. We recommend W-AFDA for the earthquake ground motion modeling in surface sedimentary structures.

In practical calculations it is desirable to obtain values of the displacement/particle velocity components directly at the free surface.

In the stress-imaging techniques it is possible to use averaging across the free surface in order to obtain the missing component(s) at the free surface, as suggested by *Gottschämmer and Olsen (2001).*

In the techniques with adjusted FD approximations it is possible to apply extrapolation formulas of different orders of accuracy. The 4th-order formula is necessary to obtain good accuracy.

Acknowledgments: The authors thank Rob Graves, Arben Pitarka and Kim Olsen for discussions on the free-surface modeling. The reviews by Heiner Igel and the anonymous reviewer helped to improve the paper. This work was supported in part by Grant No. 1/1090/21, VEGA, Slovak Republic, European Commission Project No. EVG1-CT-2000-00026 SESAME, National Science Foundation grant CDA96-01954, and by Silicon Graphics Inc. One of the authors (P. M.) thanks the Institute for Crustal Studies, University of California at Santa Barbara, for the invitation and support. ICS Contribution No. 514.

Received: January 7, 2002; *Accepted: February 20, 2002*

References

Bouchon M., 1981. A simple method to calculate Green's functions for elastic layered media. *Bull. Seismol. Soc. Amer.,* **71**, 959-971.

Coutant O., 1989. Program of numerical simulation AXITRA. Res. Rep. LGIT, Universite Joseph Fourier, Grenoble (in French).

Gottschämmer E. and Olsen K.B., 2001. Accuracy of the explicit planar free-surface boundary condition implemented in a fourth-order staggered-grid velocity-stress finite-difference scheme. *Bull. Seismol. Soc. Amer.,* **91**, 617-623.

Graves R.W., 1996. Simulating seismic wave propagation in 3D elastic media using staggered-grid finite differences. *Bull. Seismol. Soc. Amer.,* **86**, 1091-1106.

Hestholm S., 1999. Three-dimensional finite difference viscoelastic wave modelling including surface topography. *Geophys. J. Int.,* **139**, 852-878.

Hestholm S., Ruud B.O. and Husebye E.S., 1999. 3-D versus 2-D finite-difference seismic synthetics including real surface topography. *Phys. Earth Planet. Inter.,* **113**, 339-354.

Levander A., 1988. Fourth-order finite-difference P-SV seismograms. *Geophysics,* **53**, 1425-1436.

Madariaga R., 1976. Dynamics of expanding circular fault. *Bull. Seismol. Soc. Amer.*, **66**, 639-666.

Moczo P., Bystrický E., Kristek J., Carcione J.M. and Bouchon M., 1997. Hybrid modeling of P-SV seismic motion at inhomogeneous viscoelastic topographic structures. *Bull. Seismol. Soc. Amer.*, **87**, 1305-1323.

Moczo P., Kristek J. and Halada L., 2000. 3D fourth-order staggered-grid finite-difference schemes: Stability and grid dispersion. *Bull. Seismol. Soc. Amer.*, **90**, 587-603.

Moczo P., Kristek J. and Bystrický E., 2001. Efficiency and optimization of the 3D finite-difference modeling of seismic ground motion. *J. Comp. Acoustics*, **9**, 593-609.

Ohminato T. and Chouet B.A., 1997. A free-surface boundary condition for including 3D topography in the finite-difference method. *Bull. Seismol. Soc. Amer.*, **87**, 494-515.

Rodrigues D., 1993. *Large Scale Modelling of Seismic Wave Propagation*. PhD. Thesis, Ecole Centrale Paris.

Ruud B. and Hestholm S., 2001. 2D surface topography boundary conditions in seismic wave modelling. *Geophys. Prospect.*, **49**, 445-460.

Virieux J., 1984. SH-wave propagation in heterogeneous media: Velocity-stress finite-difference method. *Geophysics*, **49**, 1933-1957.

Virieux J., 1986. P-SV wave propagation in heterogeneous media: Velocity-stress finite-difference method. *Geophysics*, **51**, 889-901.